RSC Advances

ROYAL SOCIETY OF CHEMISTRY

www.rsc.org/advances

Tin oxide nanoparticles from laser ablation encapsulated in a carbonaceous matrix – a negative electrode in lithium-ion battery applications

Andrzej P. Nowak[1,*], A. Lisowska-Oleksiak[1], K. Siuzdak[2], M. Sawczak[2], M. Gazda[3], J. Karczewski[3], G. Trykowski[4],

[1]Faculty of Chemistry, Department of Chemistry and Technology of Functional Materials Gdańsk University of Technology, Narutowicza 11/12, 80-233 Gdańsk, Poland

[2] Center for Plasma and Laser Engineering, Szewalski Institute of Fluid Flow Machinery, Fiszera 14, 80-231 Gdańsk, Poland

[3] Faculty of Applied Physics and Mathematics, Gdańsk University of Technology, Narutowicza 11/12, 80-233 Gdańsk, Poland

[4] Faculty of Chemistry, Nicolaus Copernicus University in Toruń, Gagarina 7, 87-100 Toruń, Poland

[*]email: andnowak@pg.gda.pl

Abstract

This report concerns carbonaceous electrodes doped with tin (II) oxide nanoparticles. Tin nanoparticles are obtained by pulsed laser ablation in water. Crystalline nanoparticles have been encapsulated in a carbonaceous matrix formed after pyrolysis of a mixture consisting of tin/tin (IV) oxide nanoparticles and gelatine. The obtained material is characterized by means of X-ray diffraction, selected area diffraction, scanning electron microscopy, transmission electron microscopy and energy dispersive X-ray analysis. Battery charging/discharging tests exhibit a capacity of 580 mAh g^{-1} for current densities of 100 mA g^{-1}. Cycling performance of

the material suggests that the tested nanocomposite can be used as an anode for lithium-ion batteries.

Keywords: tin (II) oxide, hard carbons, laser ablation, nanoparticles, anode material, lithium-ion batteries.

1. Introduction

Lithium-ion batteries are common power sources which are used in portable electronic devices such as cameras and mobile phones. Such batteries show relatively high capacities in comparison with lead acid and Ni-MH battery systems. However, current energy demands are focused on electrode materials suitable for use in high energy applications, i.e. electric vehicles (EV). This limits the usage of graphite anodes, known to be an active material in commercial batteries. The theoretical specific capacity of graphite is 372 mAh g^{-1} with formation of LiC_6[1]. The general reactions involving the lithium insertion/extraction reversible process are given below:

$$xLi^+ + xe^- + M = Li_xM \quad (1)$$

where M is the host material i.e. carbon, silicon, tin[2].

Silicon and tin are very promising anode materials owing to their high theoretical specific capacity of 4200 and 994 mAh g^{-1}, respectively[3,4]. The problem with $Li_{4.4}Si$ and $Li_{4.4}Sn$ systems is that these anodes suffer from pulverization having an effect on the poor cycling performance, on huge volume changes and on active material contact loss during the alloying and dealloying process[5]. This limits the use of metal anodes in practical applications. Instead of metal anodes, metal oxides replace the graphite anode as they offer a high theoretical capacity [6–10] as well as other silicon[11,12] and tin[13] derivatives.

The electrochemical reaction of tin oxide with lithium ions is a two-step process:

$$SnO_2 + 4\ Li^+ + 4\ e^- \leftrightharpoons Sn + 2\ Li_2O \quad (2)$$

$$Sn + x\ Li^+ + x\ e^- \leftrightharpoons Li_xSn \qquad (0 \leq x \leq 4.4) \qquad (3)$$

with a theoretical lithium storage capacity of 781 mAh g^{-1} [14].

The SnO_2 anode suffers from the same factors as the tin metal anode. However, the latest studies show that some of these problems may be overcome by special treatment of tin oxide material, i.e.: reducing the particle size[15] or changing the morphology[16]. The capacity of the treated materials was improved but capacity fading due to volume changes was not eliminated. Thus, it is still important to increase the capacity retention problem in tin oxide anodes for practical applications.

Attempts have been made to improve the mechanical stability of tin oxide by incorporating carbonaceous materials[7,17–19]. This modification enhances capacity retention, charge/discharge current rates, active surface area, efficient contact between metal oxide particles and carbon. It also prevents volume changes during alloying/dealloying due to increase of the porosity of the material and drastically minimized diffusion length[20]. Moreover, tin does not react with carbon and the formation of tin carbide is excluded[21].

Taking into account the size of the particles, the pulsed laser ablation technique in liquid (PLAL)[22] was used to obtain a colloid of tin oxide nanoparticles. In comparison with conventional synthesis methods, PLAL allows the nanoparticles synthesis process to be simplified to obtain nanoparticles in the form of pure water based colloid without chemical additives and by-products[22,23]. Recent studies of tin oxide nanotubes obtained by PLAL show that this technique might by suitable for electrode material preparation for lithium-ion battery application [24]. However, the authors claim that tin oxide nanotubes exhibit a specific capacity which is higher than the theoretical one, which is confusing.

Here, we applied PLAL to prepare a colloid of SnO_2 nanoparticles followed by mixing with water solution of gelatin. After pyrolysis, the new material was tested as an anode material in a battery cell.

2. Experimental

Tin oxide nanoparticles in a carbon matrix ($SnO@C_{gel}$) were obtained in two steps. In the first step, the synthesis of Sn/SnO_2 nanoparticles was carried out using the experimental setup described in detail in the previous work[22]. The laser (Nd:YAG) operated at 1064 nm with 6 ns pulse duration and pulse repetition rate of 10 Hz. The laser beam was focused with a 100 mm focal length lens on a metallic tin (Sn) target immersed in deionized water. The laser energy density on the target surface was 20 J cm^{-2}. In the first stage of nanoparticle fabrication, the ablation process was carried out for 45 minutes. During ablation, the Sn target was rotating to avoid crater formation. After this stage, a brown $SnO_x \times H_2O$ colloid was obtained. In the second stage, the colloid was illuminated with UV radiation (350 nm) for 15 minutes. Exposition of the as-prepared colloid to UV radiation causes a colour change from brown to white as the result of coagulation of primary colloidal $SnO_x \times H_2O$ nanoparticles[25]. In the second step, gelatine (POCH Gliwice) was added to obtain a 5% wt. solution, followed by mixing and heating at 50°C for 2 h. The weight ratio - gelatin to Sn/SnO_2 - before pyrolysis was 100:1. The mixture was inserted into a ceramic crucible, put into a quartz tube, evacuated, subsequently filled with argon and finally heated under a steady flow of argon (Ar 5.0) (25 ml min^{-1}) in a programmable horizontal tube-furnace (Czylok, Poland) with a heating rate of 100°C/h up to 900°C, and held at the final temperature for 2 h. The pyrolysed samples were mechanically milled for 30 minutes at 1500 rpm. The electrodes were prepared from a slurry (60 wt.% of active material, 20 wt.% of carbon black (Super P, Timcal, Switzerland) and 20 wt.% of a binder (sodium carboxymethyl cellulose, Sigma-Aldrich, USA) in water on a ~ 10 μm thin copper foil (Schlenk Metallfolien GmbH & Co KG, Germany). After the tape casting procedure, the material was dried for 8 h at 100°C in an oven. Next, the discs were cut off, pressed for 30 s under 200 MPa load and dried under dynamic vacuum in an oven (Glass Oven B-595, Büchi, Germany) for 24 h at 80°C.

Dried disc electrodes were used in two-electrode Swagelok® cells with lithium foil as a counter and reference electrodes (99.9% purity, 0.75 mm thickness, AlfaAesar, USA), 1 M $LiPF_6$ in EC:DMC ratio 1:1 (LP30 Merck, Germany) as the electrolyte, and glass fibre (Schleicher&Schüll, Germany) as the separator.

The battery tests of the samples were performed using the ATLAS 0961 MBI (Poland) multichannel battery testing sstem with different current densities. Cyclic voltammetry measurements (CV) were carried out on a PGSTAT302N galvanostat/potentiostat over the potential range 0.005 ÷ 3 V *vs*. Li/Li^+ with a scanning rate of 0.1 mV s^{-1}.

The phase composition of the samples was investigated by an X-Ray diffraction system in the range of 2θ = 20 - 70°, using an X-ray diffractometer (Xpert PRO-MPD, Philips) with copper K_α radiation (λ = 1.5404 Å).

Thermal gravimetric analysis (TGA) and differential scanning calorimetry (DSC) were performed by NETZSCH STA 449F1. Approximately 5 mg of sample was heated from 25C to 900C at a ramp rate of 15 C min^{-1} in argon at a flow rate of 40 ml/min.

The morphology of the samples was investigated by the Schottky field emission scanning electron microscopy (FEI Quanta FEG 250) with an ET secondary electron detector. The beam accelerating voltage was kept at 20 kV. For the purpose of elemental analysis, the Energy Dispersive X-ray Spectroscopy was performed with the EDAX Genesis APEX 2i with the ApolloX SDD spectrometer, in particular areas of each sample.

The samples for the TEM analysis had first been suspended in absolute ethyl alcohol (99.8% pure p.a.) and sonicated in an ultrasonic bath (InterSonic IS-1K) for 5 seconds. After that, the solutions were prepared for analysis by placing a drop (4 µl) on carbon-coated copper grids (Plano, type: Lacey Cu 400 mesh), allowing the solvent to evaporate at room temperature. To obtain information about the particle size, shape, dispersion uniformity and chemical composition, the samples were analysed with a transmission electron microscope with an

energy-dispersive X-ray spectrometer (TEM-EDX, Tecnai F20 X-Twin, FEI and EDAX spectrometer).

3. Results and discussion

3.1. TGA and DSC

Figures 1a and 1b show the TG and DSC analysis of pure gelatin and a mixture gelatin/nSnO, respectively. The main peak in Fig. 1a, seen at 160.1°C, corresponds to water and other volatile products evaporation from the aqueous solution of gelatin. The total mass loss is ~ 72.4%. At 310°C, further gas evolution occurs with the mass change of 3.74%. There is a small peak at ~ 300°C that corresponds to N-O-C volatile products coming from gelatin. These might be urethane-based gaseous chemicals [26].

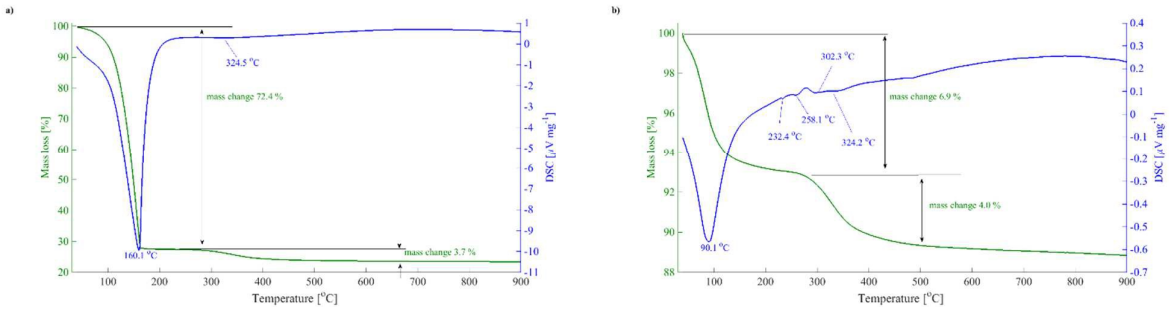

Fig. 1. TGA and DSC analysis at 15 C min^{-1} for a) gelatin, b) gelatin/nSnO.

The TGA spectrum of the mixture gelatin/nSnO is shown in Fig. 1b. The main peak is at 90.1°C. This peak is very likely attributed to water evaporation and removing of other volatile side products coming from gelatine. We assume that the tin/tin oxide nanoparticles act as a catalyst and hence the main peak in Fig. 1b is shifted about 80°C towards the lower temperature in comparison to the peak in Fig. 1a (160.1°C). The peak at 232.4°C corresponds to a phase change of tin from solid to liquid form[27]. The peaks at 258.1°C, 280.7°C might origin from the formation of SnO_x as no change in mass is observed. The maxima at 302.3°C and 324.2°C are very likely attributed to some volatile products of N-O-C consisted

compounds obtained after pyrolysis of the gelatin aqueous solution in the presence of tin/tin oxide nanoparticles.

3.2. XRD

The XRD results with the reference data are presented in Fig. 2 (line a-e): the XRD pattern of the Sn/SnO_2 nanoparticles obtained with the ablation technique is given as (a), the reference pattern of Sn as (b), SnO_2 as (c), SnO and Sn_5O_6 as (d) and the studied $SnO@C_{gel}$ material annealed at 900°C as (e). The comparison of XRD patterns of the material obtained from metallic tin after laser ablation with reference patterns (00-004-0673 and 00-041-1445) indicates the presence of tin and tin (IV) oxide.

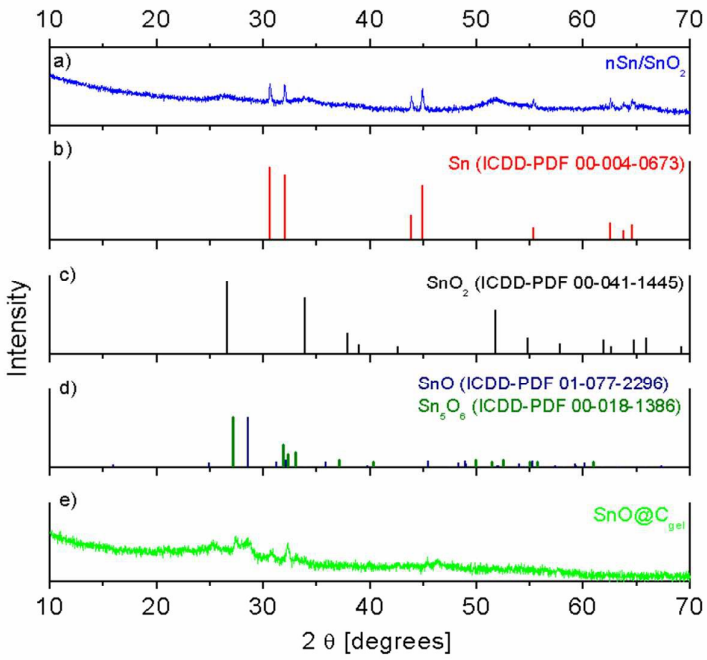

Fig. 2. (a) XRD diffractogram of Sn/SnO_2 nanoparticles prepared by the PLD technique, (b) XRD diffractogram calculated on data taken from the International Centre for Diffraction Data Powder Diffraction File (ICDD-PDF) for reference pattern of Sn (00-004-0673), (c) SnO_2 (00-041-1445), (d) SnO (01-077-2296) and Sn_5O_6 (00-018-1386) and (e) XRD diffractogram of the $SnO@C_{gel}$ material annealed at 900 °C.

Thus, our results show that laser ablation of metallic tin in water gives a mixture consisting of nanoparticles of tin and nanoparticles of tin (IV) oxide as is shown in Ref.[28]. The signal coming from SnO_2 is relatively low and broad due to the amorphous structure of SnO_2. The SnO_2 might be in its meta-stable state but still keeping the short range order.

According to the literature, the origin of SnO_2 formation is explained in the following way: tin particles are oxidized by ionization energy while water molecules are ionized with formation of OH^- ions. The scheme of SnO_2 formation is given below [29]:

$$Sn^{4+} + 4OH^- \rightarrow Sn(OH)_4 \quad (4)$$

$$Sn(OH)_4 \xrightarrow{\text{laser ablation (heating)}} SnO_2 + H_2O \quad (5)$$

According to authors of Ref.[29], the presence of positively charged tin nanoparticles and negatively charged hydroxide ions is the force leading to the formation of tin (IV) hydroxide. The heat from laser ablation causes dehydratation of $Sn(OH)_4$ and tin (IV) oxide appears in the aqueous solution[29].

It is known that the liquid formed by laser ablation is typically a colloidal one. Thus, we claim that at the beginning, laser ablation of Sn leads to formation of Sn^{2+} ions that react with OH^- ions coming from water ionization. Tin (II) hydroxide $Sn(OH)_2$ ($SnO \times H_2O$) is the final product after PLAL. Considering charged colloidal particles formation during ablation one would expect that the central part, the nuclei of the colloidal particle should rather be $SnO \times H_2O$ nanoparticles with adsorbed $Sn(OH)^+$ in the first zone and OH^- in the second zone:

$$\{m[SnO \times H_2O] \cdot nSn(OH)^+ \cdot (n-x)OH^-\} \cdot xOH^- \quad (6)$$

The sequence also may be different – we did not perform studies allowing the charge of colloidal particles in the formed fluid to be determined.

UV radiation leads to coagulation of the colloidal system and the disproportion reaction with formation of Sn and SnO_2 particles in two steps according to reactions given in Ref.[30]:

$$3SnO \rightarrow Sn_2O_3 + Sn \quad (7)$$

$$2Sn_2O_3 \rightarrow 3SnO_2 + Sn \quad (8)$$

Nanoparticles of metallic tin and tin (IV) oxide are the final products of laser ablation and UV treatment. It is worth emphasizing that presence of Sn(II) species in the colloidal liquid, instead of proposed Sn(IV) as given in Ref.[29], is crucial to obtain both Sn(IV) and Sn(0) during dismutation reactions (7,8).

The XRD pattern of a mixture consisting of Sn/SnO_2 nanoparticles and the source of carbon followed by pyrolysis at 900ºC is shown in Fig. 2e. Small reflections seen in the XRD pattern may be attributed to tin (II) oxide (see Fig. 2d). The lack of Sn and SnO_2 is very likely caused by the chemical oxidation of tin with reduction of SnO_2 at the same time, according to reaction:

$$Sn + SnO_2 \rightarrow 2\,SnO \quad (9)$$

3.3. SEM EDX

In Fig. 3., the SEM images of the $SnO@C_{gel}$ electrode material are shown. The morphology of the material shows that it consists of polyhedron shaped elements covered with spherical particles. The average grain size of these domains is less than 5 μm for the former, while the diameter of the latter is below 80 nm.

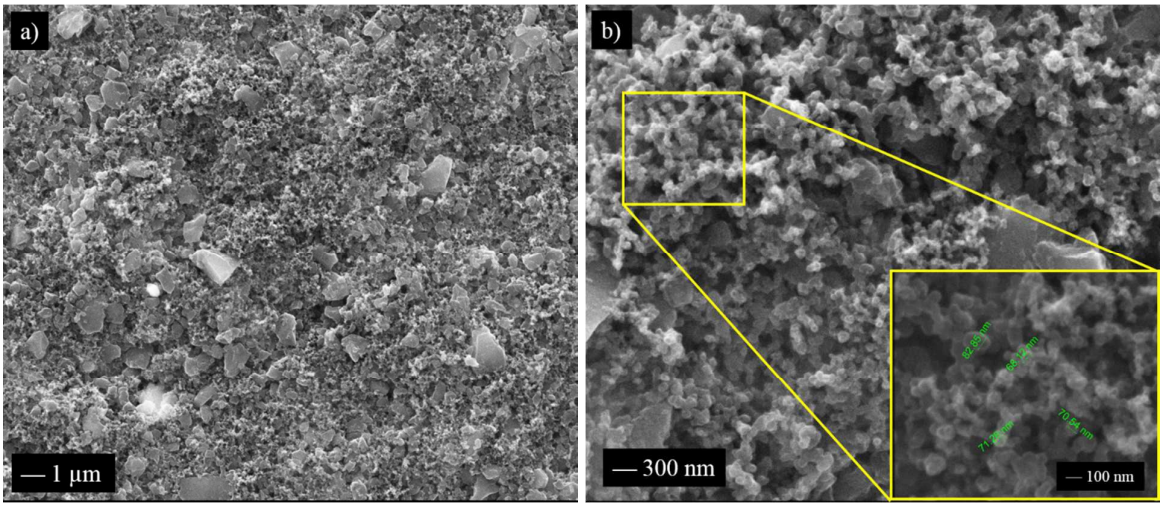

Fig. 3. The SEM images of the SnO@C_{gel} electrode material at different magnification.

The SEM-EDX mapping of the SnO@C_{gel} electrode points to polyhedron shape particles being of carbonaceous origin, while the spherical shaped part is inorganic. The main signal comes from carbon and the signal of tin is quite weak (inset in Fig. 4a). This was expected as the ratio of gelatin to Sn/SnO_2 nanoparticles before pyrolysis was 100:1.

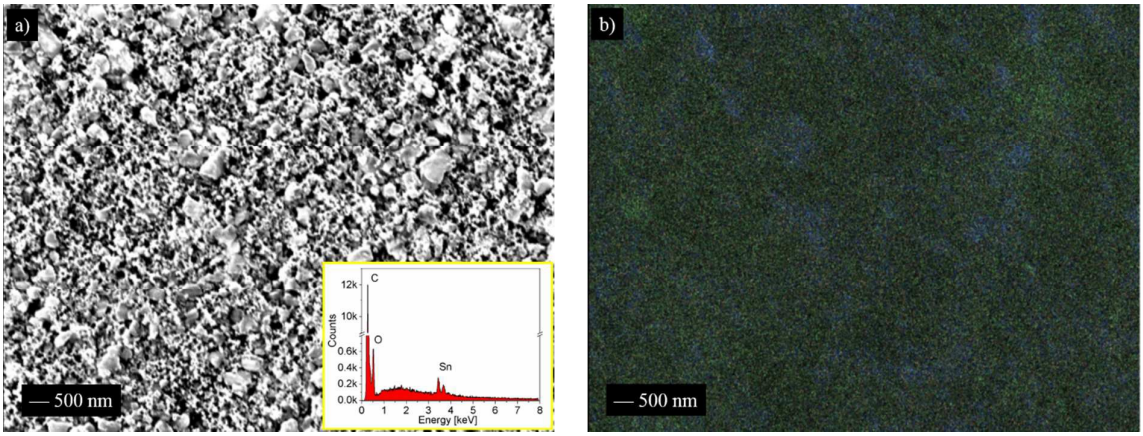

Fig. 4. SEM image of the SnO@C_{gel} surface with EDX analysis (a) EDX mapping of the sample (O blue, Sn green) (b).

The SEM-EDX mapping of oxygen (blue) and tin (green), shown in Fig. 4b, evidences that both elements are present in the sample. The area of more intense green colour may suggest the presence of metallic tin particles. The presence of tin oxide is expected at blue sites. The close neighbourhood of tin (green) and oxygen (blue) atoms confirms the XRD results that tin oxide was formed after thermal treatment. Also, it may be concluded that the electrode material consists of C, Sn and O elements but distribution of the inorganic nanoparticles is not homogenous within the whole material.

3.4. TEM

The TEM image of SnO@C_{gel} is shown in Fig. 5. The diameter of the SnO nanoparticles is less than 100 nm and tin oxide is almost uniformly dispersed in the carbonaceous matrix.

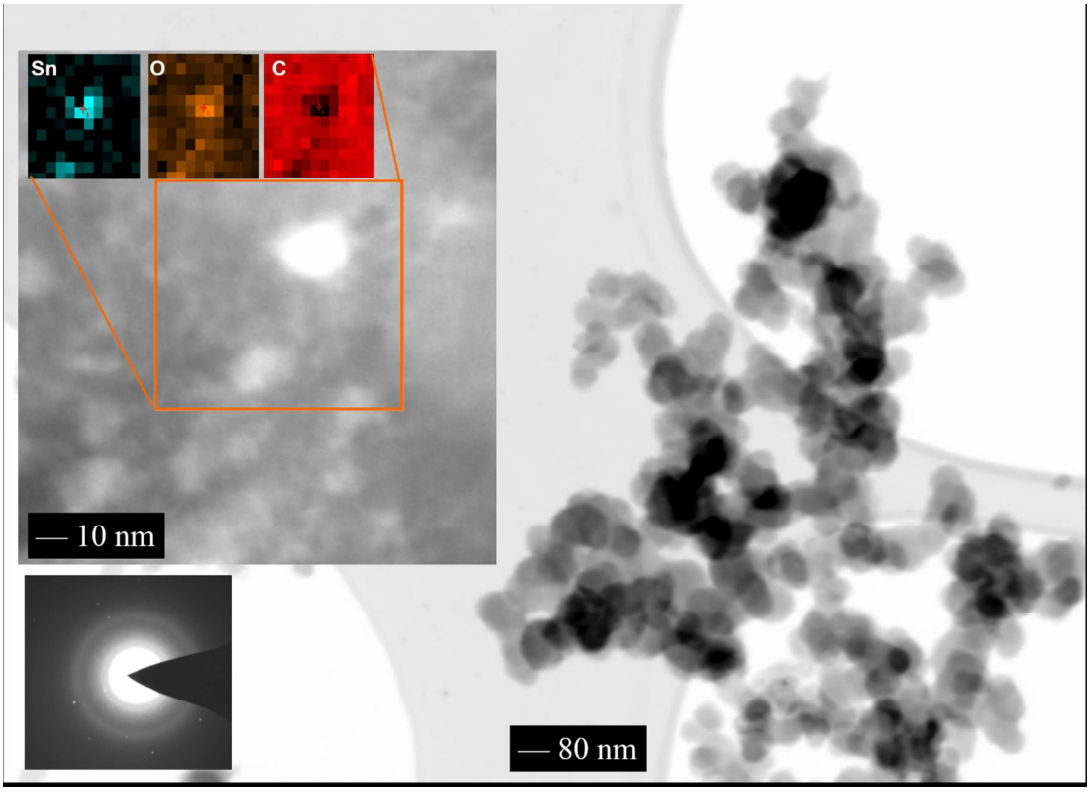

Fig. 5. TEM micrograph of the SnO@C_{gel} electrode material; inset: EDX analysis (upper left corner) and SEAD (bottom left corner).

In the inset, the TEM-EDX mapping evidences the presence of SnO nanoparticles. It can be clearly observed that the Sn element is bonded with the O element as both of them occupy the same place. SnO is in the form of an island surrounded by carbon. The selected area diffraction pattern (SEAD) proves the presence of crystalline tin (II) oxide and amorphous carbon. These results are in agreement with the XRD pattern shown in Fig. 2.

3.5. Electrochemistry

The cyclic voltammetry (cv) curves of SnO@C_{gel} in the potential range from 0.005 to 3.0 V *vs*. Li/Li^+ are shown in Fig. 6. On the first cv scan, the cathodic current increase starting at 0.9 V is attributed to the solid electrolyte interphase (SEI) formation at the surface of the electrode[31]. SEI formation is accompanied by Faradaic charge transfer. It is known that for tin

oxides (SnO_2 and SnO) reacting with lithium ions two processes may occur: the first one is SnO_2/SnO conversion to Sn and Li_2O and the second one is alloy Li_xSn formation [32,33].

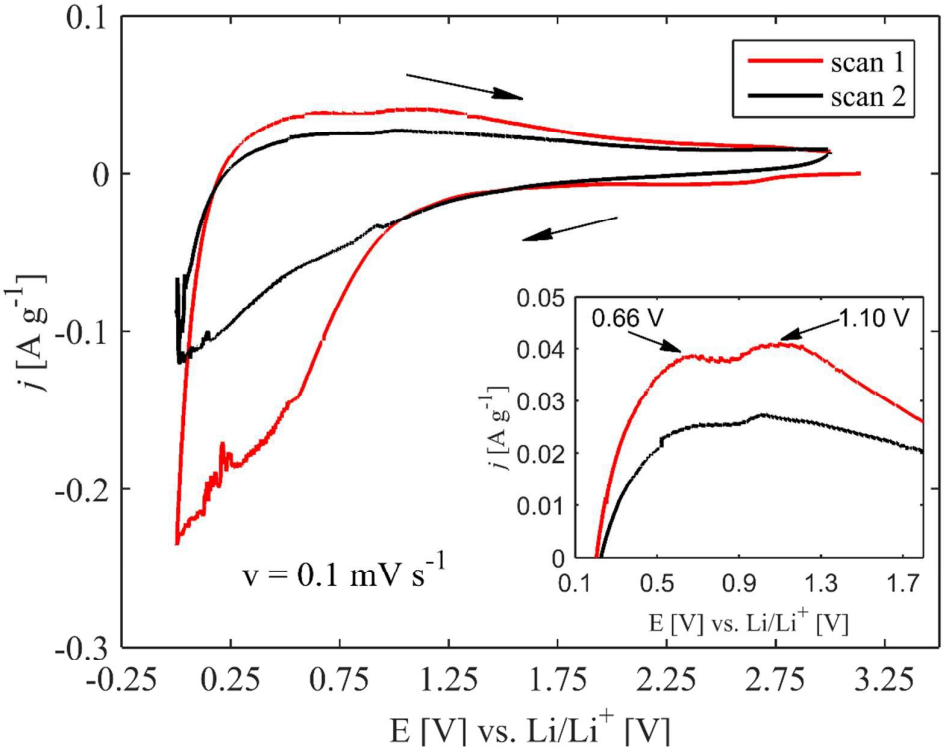

Fig. 6. The first two cyclic voltammetry (cv) curves of the SnO@C_{gel} at sweep rate v = 0.1 mV s^{-1}.

On the anodic branch of the cv curve two small humps are recorded at 0.66 and 1.10 V. The former is very likely to be attributed to de-alloying of Sn_xLi, the latter originates from the reversible reaction between lithium ions and tin oxide[19,32,34].

Taking into account both anodic reactions from the first cycle it could be assumed that the conversion reaction (eq. 10) occurs up to potential 0.85 V. This is the potential between both anodic current maxima where the current reaches a minimum. Below potential E = 0.85 V alloying occurs:

$$SnO + 2\,Li^+ + 2\,e^- \leftrightharpoons Sn + Li_2O \qquad (0.85 - 3.0\ V) \qquad (10)$$

$$Sn + x\,Li^+ + x\,e^- \leftrightharpoons Li_xSn \qquad (0.005 - 0.85\ V) \qquad (3)$$

The anodic process during the second cycle is less visible. It is very likely due to the presence of the pyrolysed carbonaceous material, which is in excess in comparison with SnO nanoparticles. Such a shape of the cv curve is typical for supercapacitors based on carbonaceous electrode materials charged at higher current rates[35,36].

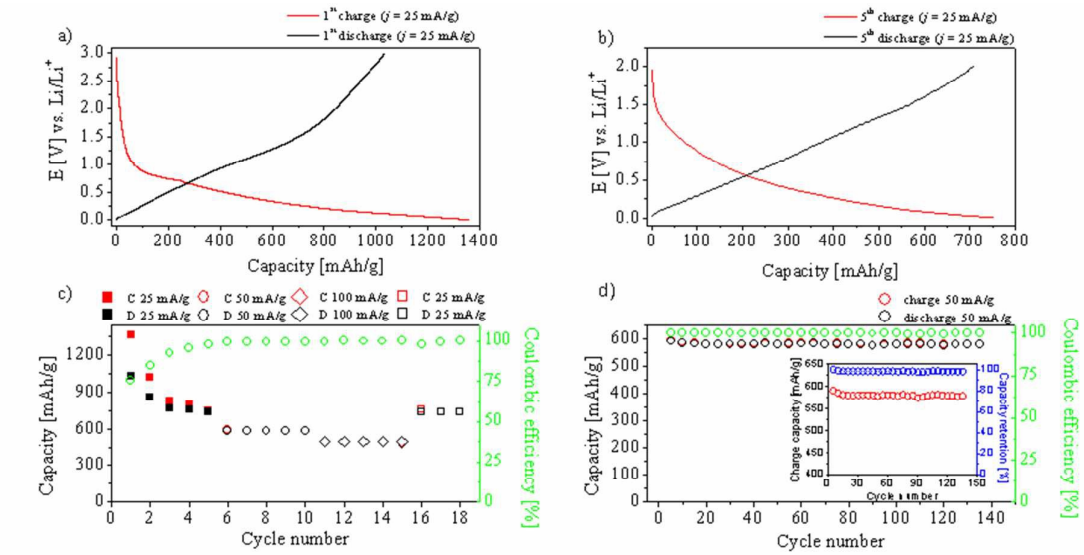

Fig. 7. Electrochemical performance of the SnO@C_{gel} electrode material: a) first charging/discharging curve, b) fifth charging/discharging curve, c) specific capacity vs. cycle number at different current rates, d) extended cycling at 50 mA g^{-1}.

The first and fifth charge/discharge curves of SnO@C_{gel} material are shown in Fig. 7 a,b. The first specific charge and discharge capacities are 1370 and 1070 mAh g^{-1}, respectively. The capacity loss of 300 mAh g^{-1} gives the capacity retention of 78% after the first lithium ions insertion/extraction, as expected. This loss is related to SEI formation and is confirmed by the cv result (see Fig. 6.). For the fifth cycle, the charge/discharge specific capacities are almost the same and equal to 753 mAh g^{-1} for charging and 739 mAh g^{-1} for discharging.

The specific capacity in the function of cycle number at different values of applied current density is presented in Fig. 7c. Although the specific charge capacity for 25mA g^{-1} drops from 1370 to 753 mAh g^{-1}, the material exhibits good capacity retention, equal to 96%, from the 3rd to the 5th cycle. Even better efficiency is recorded for the electrode material charged and

discharged at 50 mA g^{-1}. The capacity retention after 5 cycles is 98.3% with the capacity of 582 mAh g^{-1}. Much better results are obtained for further charging at the same current density, see Fig. 7d. After another 140 cycles the average specific capacity is 580 mAh g^{-1} with capacity fading of 2% (see inset in Fig. 6d). This capacity is higher by ~ 180 mAh g^{-1} in comparison with the data obtained by Gerbaldi *et.al.* for tin oxide with mesoporous carbon spheres (SnO_2/MCS)[34] and higher than for SnO_2/MWCNTs buckypaper obtained by the sol-gel method[37] for the same current density. However, the specific capacity of SnO@C_{gel} at 50 mA g^{-1} is lower in comparison with results shown by Lee for hollow core-shell SnO_2 nanoparticles[38]. The lower capacity may originate from a smaller amount of tin and tin oxide nanoparticles mixed with an aqueous solution of gelatine in the studied case. The charging/discharging test of the material for a current density of 100 mA g^{-1} shows specific capacities of 498 mAh g^{-1} for the first charge and 495 mAh g^{-1} for the fifth discharge. It gives capacity retention of 99.4%. Similar results were obtained by Guo *et. al.* for SnO_2/MWCNT[14]. When the low current density (25 mA g^{-1}) was applied again, the specific capacity for charging and discharging after the last (third) cycle was 735 mAh g^{-1} and 734 mAh g^{-1}, respectively. This proves that the electrode material is stable during the cycling protocol, 5 x 25 mA g^{-1} → 5 x 50 mA g^{-1} → 5 x 100 mA g^{-1} → 3 x 25 mA g^{-1}, and maintains the specific capacity at high values.

The results obtained suggest that two factors influence the electrochemical performance of the SnO@C_{gel} electrode material. The first is the presence of SnO nanoparticles and the second is the occurrence of the carbonaceous matrix. In our previous study we showed that pyrolysed gelatine exhibits a capacity of only 343 mAh g^{-1} even for a current density equal to 18.6 mA g^{-1} (C/20 – current rate)[39]. Thus, the nanoparticles enhance the specific charge/discharge capacity while the pyrolysed organic source of carbon stabilizes the cyclability of the electrode material. Our results are in agreement with the results obtained by other authors

who proved that modification of tin/tin oxide by carbonaceous materials has a positive impact on the electrochemical stability of such a complex system[4,7,8,14,16,17,33,34,37,40,41]. Our studies have shown that the use of PLA followed by UV irradiation methods allow the preparation of suitable nanostructures in a simple and reproducible way.

4. Conclusions

We have obtained SnO nanoparticles by laser ablation of metallic tin followed by pyrolysis with a hard carbon precursor – gelatin ($SnO@C_{gel}$). Sn/SnO_2 nanoparticles were obtained by the pulsed laser ablation technique resulting in a diameter of the particles below 100 nm after thermal treatment. During the annealing procedure in the oven, Sn/SnO_2 nanoparticles were transformed into SnO.

The morphology and composition of the material were performed with the use of XRD, SEAD, SEM and TEM. The XRD and SEAD studies confirmed the presence of crystalline SnO and amorphous carbon.

The $SnO@C_{gel}$ electrode material exhibits very stable cycling electrochemical performance and rate capability. The material shows a specific capacity of 580 mAh g^{-1} with capacity retention over 98% after 140 cycles. The presence of SnO in the carbon matrix improves the materials' characteristics in terms of its usage for application as a negative electrode in lithium-ion batteries.

Acknowledgments

The authors gratefully acknowledge the financial support from the Ministry of Science and Higher Education (DS no. 030893/003).

References

1 B. M. Winter, J. O. Besenhard, M. E. Spahr and P. Novak, *Adv. Mater.*, 1998, 725–763.

2 G. Neumann and A. Würsig, *Phys. Status Solidi RRL*, 2010, **4**, A21–A23.

3 J. Graetz, C. C. Ahn, R. Yazami and B. Fultz, *Electrochem. Solid-State Lett.*, 2003, **6**, A194.

4 Y. Yu, L. Gu, C. Zhu, P. a van Aken and J. Maier, *J. Am. Chem. Soc.*, 2009, **131**, 15984–5.

5 H. Li, L. Shi, Q. Wang, L. Chen and X. Huang, 2002, **148**, 247–258.

6 M. Behm and J. T. S. Irvine, *Electrochim. Acta*, 2002, **47**, 1727–1738.

7 W.-H. Qu, F. Han, A.-H. Lu, C. Xing, M. Qiao and W.-C. Li, *J. Mater. Chem. A*, 2014, **2**, 6549.

8 J. Ren, J. Yang, A. Abouimrane, D. Wang and K. Amine, *J. Power Sources*, 2011, **196**, 8701–8705.

9 W.-S. Chang, C.-M. Park, J.-H. Kim, Y.-U. Kim, G. Jeong and H.-J. Sohn, *Energy Environ. Sci.*, 2012, **5**, 6895–6899.

10 N. Yan, F. Wang, H. Zhong, Y. Li, Y. Wang, L. Hu and Q. Chen, *Sci. Rep.*, 2013, **3**, 1568–1574.

11 M. Wilamowska, M. Graczyk-Zajac and R. Riedel, *J. Power Sources*, 2013, **244**, 80–86.

12 L. M. Reinold, M. Graczyk-Zajac, Y. Gao, G. Mera and R. Riedel, *J. Power Sources*, 2013, **236**, 224–229.

13 J. Kaspar, C. Terzioglu, E. Ionescu, M. Graczyk-Zajac, S. Hapis, H.-J. Kleebe and R. Riedel, *Adv. Funct. Mater.*, 2014, **24**, 4097–4104.

14 G. Du, C. Zhong, P. Zhang, Z. Guo, Z. Chen and H. Liu, *Electrochim. Acta*, 2010, **55**, 2582–2586.

15 M. Noh, Y. Kim, M. G. Kim, H. Lee, H. Kim, Y. Kwon, Y. Lee and J. Cho, *Chem. Mater.*, 2005, 3320–3324.

16 S. Oro, K. Urita and I. Moriguchi, *Chem. Commun.*, 2014, **50**, 7143–6.

17 S. Li, Y. Wang, J. Qiu, M. Ling, H. Wang, W. Martens and S. Zhang, *RSC Adv.*, 2014, **4**, 50148–50152.

18 Y. Yu, L. Gu, C. Wang, A. Dhanabalan, P. A. van Aken and J. Maier, *Angew. Chem. Int. Ed. Engl.*, 2009, **48**, 6485–9.

19 D. R. Chojnacka A., Molenda M., Bakierska M., *ECS Trans.*, 2015, **64**, 165–171.

20 G. Zhou, D.-W. Wang, L. Li, N. Li, F. Li and H.-M. Cheng, *Nanoscale*, 2013, **5**, 1576–82.

21 A. R. Kamali and D. J. Fray, *Rev. Adv. Mater. Sci.*, 2011, **27**, 14–24.

22 K. Siuzdak, M. Sawczak, M. Klein, G. Nowaczyk, S. Jurga and A. Cenian, *Phys. Chem. Chem. Phys.*, 2014, **16**, 15199–206.

23 M.-Z. Xue, J. Yao, S.-C. Cheng and Z.-W. Fu, *J. Electrochem. Soc.*, 2006, **153**, A270.

24 Z. Liu, Z. Cao, B. Deng, Y. Wang, J. Shao, P. Kumar, C. R. Liu, B. Wei and G. J. Cheng, *Nanoscale*, 2014, **6**, 5853–5858.

25 Z. Tian, C. Liang, J. Liu, H. Zhang and L. Zhang, *J. Mater. Chem.*, 2011, **21**, 18242.

26 J.-T. Yeh and Y.-C. Shu, *J. Appl. Polym. Sci.*, 2010, **115**, 2616–2628.

27 P.-L. Sun, S.-P. Wu and T.-S. Chin, *Mater. Lett.*, 2015, **144**, 142–145.

28 O. R. Musaev, M. S. Driver, E. A. Sutter, A. N. Caruso, J. M. Wrobel and M. B. Kruger, *Appl. Phys. A*, 2013, **113**, 355–359.

29 Z. Liu, Z. Cao, B. Deng, Y. Wang, J. Shao, P. Kumar, C. R. Liu, B. Wei and G. J. Cheng, *Nanoscale*, 2014, **6**, 5853–8.

30 M. S. Moreno, R. C. Mercader and a G. Bibiloni, *J. Phys. Condens. Matter*, 1992, **4**, 351–355.

31 Y. NuLi, J. Yang and Z. Jiang, *J. Phys. Chem. Solids*, 2006, **67**, 882–886.

32 K. Kisu, M. Iijima, E. Iwama, M. Saito, Y. Orikasa, W. Naoi and K. Naoi, *J. Mater. Chem. A*, 2014, **2**, 13058.

33 H. Yamaguchi, S. Nakanishi, H. Iba and T. Itoh, *J. Power Sources*, 2015, **275**, 1–5.

34 F. Di Lupo, C. Gerbaldi, G. Meligrana and S. Bodoardo, *Int. J. Electrochem. Sci.*, 2011, **6**, 3580–3593.

35 E. Frackowiak, *J. Braz. Chem. Soc.*, 2006, **17**, 1074–1082.

36 Z.-L. Wang, D. Xu, H.-G. Wang, Z. Wu and X.-B. Zhang, *ACS Nano*, 2013, **7**, 2422–30.

37 H. Köse, A. O. Aydin and H. Akbulut, *Appl. Surf. Sci.*, 2013, **275**, 160–167.

38 D. Deng and J. Y. Lee, *Chem. Mater.*, 2008, **20**, 1841–1846.

39 A. P. Nowak, K. Trzciński and A. Lisowska-Oleksiak, *Adv. Mater. Sci.*, 2014, **14**, 75–81.

40 Y. Wang, D. Su, C. Wang and G. Wang, *Electrochem. commun.*, 2013, **29**, 8–11.

41 J. Chen and K. Yano, *ACS Appl. Mater. Interfaces*, 2013, **5**, 7682–7687.